JMEPEG (2021) 30:6640–6649
https://doi.org/10.1007/s11665-021-05944-5

1059-9495/$19.00

Effect of Laser Power on the Microstructure and Mechanical Properties of 2319-Al Fabricated by Wire-Based Additive Manufacturing

Zhaodong Zhang, Zicheng Ma, Shengbin He, Gang Song, and Liming Liu

Submitted: 17 December 2020 / Revised: 7 May 2021 / Accepted: 15 May 2021 / Published online: 3 June 2021

2319 Al alloy sample was fabricated by using low-power pulsed laser-induced MIG arc additive manufacturing. To investigate the effect of laser power on the deposited specimens, the microstructure evaluation and mechanical properties of deposited specimens were studied. With the laser power increased, the stirring effect of the laser on the molten pool was enhanced. As a result, the forming quality of the deposited samples was improved, grains were refined, and the crystal grains were fine equiaxed crystals. The micro-hardness of the sample with 300 W laser was 88.8 HV0.2, with an increase of 11.2% compared to that without laser. The tensile strength in the vertical and horizontal direction was 268 $\pm$ 5 and 279 $\pm$ 4 MPa, which were 19 and 20.1% higher than that without laser. The improved mechanical properties were due to grain refinement and microstructure improvement.

Keywords additive manufacturing, aluminum alloy, laser power, mechanical properties

1. Introduction

The 2319-Al alloy is a high-strength aluminum alloy. It has a high specific strength, excellent fatigue property, and good weldability, which is widely used in aerospace and defense (Ref 1, 2). Conventional manufacturing of 2319-Al alloy structural parts is smelting-casting or plastic deformation methods, which are not suitable for producing complicated structures (Ref 3). Additive manufacturing (AM) technology is considered to be a promising intelligent manufacturing technology because of its high efficiency and low cost (Ref 4, 5). Compared with traditional processing technology, it can reduce the production process, shorten the processing cycle, which is especially suitable for low cost and small batch of complicated structures (Ref 6). The traditional AM heat source for metal structural parts can be divided into three categories: laser, electron beam, and arc (Ref 7). The laser is widely used in AM as a heat source, which conveniently manufactures components with complex shapes (Ref 8-10). The electron beam as a heat source of AM also can fabricate high precision parts with complex shapes (Ref 11, 12). The aluminum alloy deposited process is very challenging because it is sensitive to pores and cracks (Ref 13). Karg et al. (Ref 14) reported that the crack-free Al-Cu specimens were printed by SLM. However, the ultimate tensile strength was only 235 MPa.

The wire and arc additive manufacturing (WAAM) technology uses metal wire as the filling material and arc as the heat source to fabricate metal structures by layer-by-layer welding (Ref 15, 16). Compared with laser and electron beam additive manufacturing, WAAM has the advantages of high production efficiency and low equipment cost. It is very suitable for fabricating large structures with low precision requirements (Ref 17). Some problems in WAAM also need to be solved, such as heat accumulation leading to excessive grain size. Bai et al. found that the grain size of the 2219-Al sample deposited by the TIG method was approximately 50 μm (Ref 18). Cong et al. deposited samples by CMT process and eliminated pores effectively, and so the tensile strength of Al-Cu alloy reached 248 MPa (Ref 19). Lei et al. reported that the GMAW-based AM technology has a high deposition rate and is more suitable for manufacturing large metal structural parts than GTAW and PAW (Ref 20).

Laser-MIG hybrid additive manufacturing method combines the advantages of laser and arc, it can realize high-precision and high-efficiency additive manufacturing. Because of the laser-arc synergy effects, the stability of arc improves, which has a great prospect in the manufacture of high-precision and crack-free parts (Ref 21). Zhang et al. (Ref 22) optimized process parameters to fabricate 5356-Al samples by laser-MIG and improved the forming quality of structures. However, researchers mainly focused on the macrostructure of the deposited samples, and there are few studies on the microstructure evolution or the relationship between microstructure and mechanical properties.

Laser plays a very important role in laser-MIG additive manufacturing. However, few studies are focusing on how laser power affects the microstructure and properties of structures. To prepare specimens with excellent mechanical properties, this

This invited article is part of a special topical focus in the Journal of Materials Engineering and Performance on Additive Manufacturing. The issue was organized b y Dr. William Frazier, Pilgrim Consulting, LLC; Mr. Rick Russell, NASA; Dr. Yan Lu, NIST; Dr. Brandon D. Ribic, America Makes; and Caroline Vail, NSWC Carderock.

Zhaodong Zhang, Zicheng Ma, Shengbin He, Gang Song, and **Liming Liu**, School of Materials Science and Engineering, Dalian University of Technology, Dalian 116024, People's Republic of China; and Key Laboratory of Liaoning Advanced Welding and Joining Technology, Dalian University of Technology, Dalian 116024, People's Republic of China. Contact e-mail: skyezzd@dlut.edu.cn.

paper focused on 2319-Al alloy samples fabricated by different laser power with laser-MIG hybrid additive manufacturing. In this study, the forming quality of the deposited sample is studied. The grain size and precipitates are systematically characterized. The microhardness and mechanical properties are analyzed in correlation with the changes in microstructure. And the most suitable laser power is found.

2. Experimental Details

2.1 Experimental System

This experiment uses a self-built low-power pulsed laser-induced MIG arc additive manufacturing system. This system consists of a welding platform, a pulsed laser generator with a maximum power of 800 W(type Riton LWS-800FK), and a MIG welder (type OTC WB-P500L). The schematic diagram of the system is shown in Fig. 1. The laser generator and the MIG welder are combined by a welding robot (type OTC FD-V20), and the movement of the heat source is driven by the movement of the welding robot to complete the deposition of each layer.

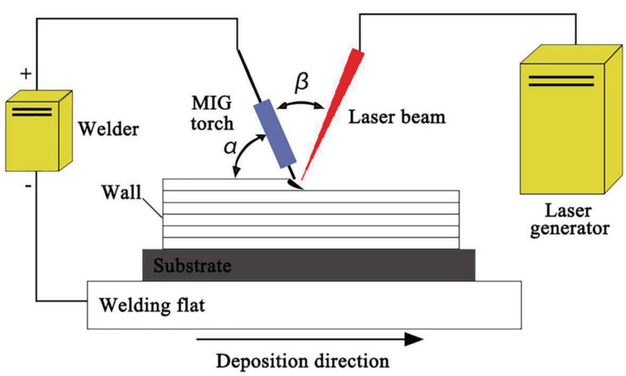

Fig. 1. Schematic diagram of the additive manufacturing system

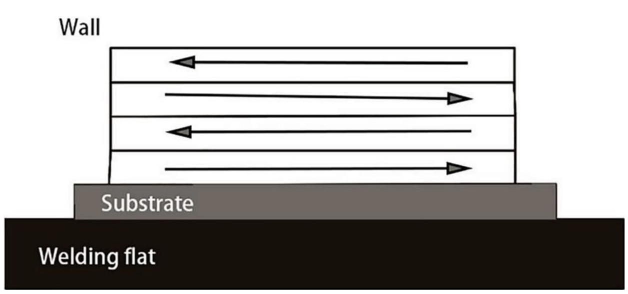

Fig. 2. Schematic diagram of the process of additive manufacturing

The angle α of the welding torch is fixed at 70°, and the angle β between the laser beam and the welding torch is maintained at 45°. This experiment adopts the method of back-and-forth depositing, and the depositing direction is changed whenever a stack of walls is completed to avoid inconsistency between the height of the arcing position and the arc extinction position. The AM process of this experiment is shown in Fig. 2.

2.2 Arrangement of the Experiments

In this experiment, ER2319 is deposited on a 2219-Al substrate. The wire has a diameter of 1.2 mm. Table 1 shows the chemical composition of the wire and substrate. Ar with a purity of 99.99% is used as shielding gas, and its flow rate is 20 L/min. The substrate and the wire with sandpaper are polished before welding. Then, it's washed with acetone to remove the oil on the surface. The welding parameters of each layer remain the same during welding. To study the effects of different laser powers on deposited samples, laser powers of 0, 100, 200, 300, and 400 W are used. The scan speeds are 400 and 450 mm/min. The welding current is 120 A, and the wire feeding speed is 720mm/min. And the residence time between adjacent layers is 60 s.

The electronic universal testing machine CSS-44100 is used for the tensile test, the test pieces of the tensile test are processed in accordance with the position shown in Fig. 3, and deposited specimens are processed into metallographic samples.

The microstructure is observed using an optical microscope (type GDM-82980) and a scanning electron microscope (type ZEISS-SUPRA 55). The hardness at different locations of the wall is tested using a model hardness tester with a load and time of 0.2 kg and 10 s, respectively.

3. Results and Discussions

3.1 Macro Morphology

Figure 4 shows the morphology of single-layer deposited samples without laser; Fig. 4(a) shows the sample morphology with the scanning speed of 400 mm/min; and Fig. 4(b) shows the sample morphology with the scanning speed of 450mm/min. It can be found that the deposited layer isn't uniform in Fig. 4(b). When the scanning speed reduces to 400mm/min, the deposited layer becomes more uniform, and the forming quality improves. When the scanning speed is high, thermal input is less and the liquid metal solidifies without enough time to spread around (Ref 23), so it's difficult to deposit more layers. When the scanning speed reduces, the heat input of the molten pool increases, the molten pool spreads around, and the deposited layer becomes uniform. Therefore, the scanning speed is 400 mm/min without the addition of a laser.

Table 1 Chemical composition of materials in weight percentage

Materials	Cu	Si	Mn	Fe	Zr	V	Ti	Zn
ER2319	5.8-6.8	0.04	0.2-0.4	0.3	0.1-0.25	0.07	0.1-0.2	≤ 0.1
2219	5.8-6.8	0.20	0.2-0.4	0.3	0.1-0.25	0.08	0.02-0.10	≤ 0.1

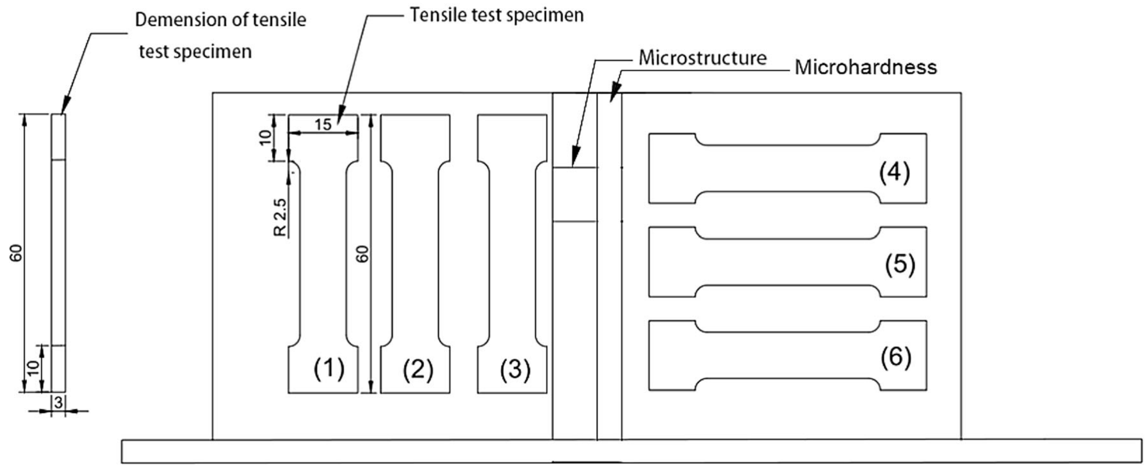

Fig. 3. Sampling position and dimensions of tensile sample

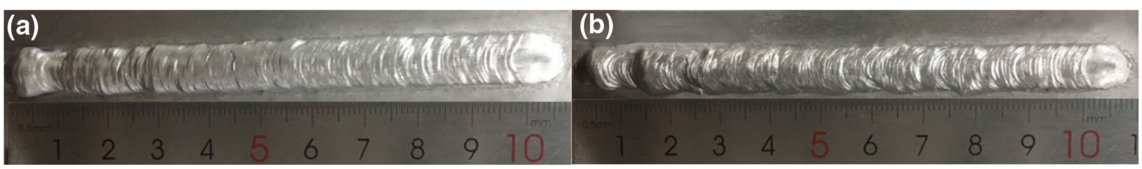

Fig. 4. Morphology of **s**ingle layer without the addition of laser: (a) 400mm/min;(b) 450 mm/min

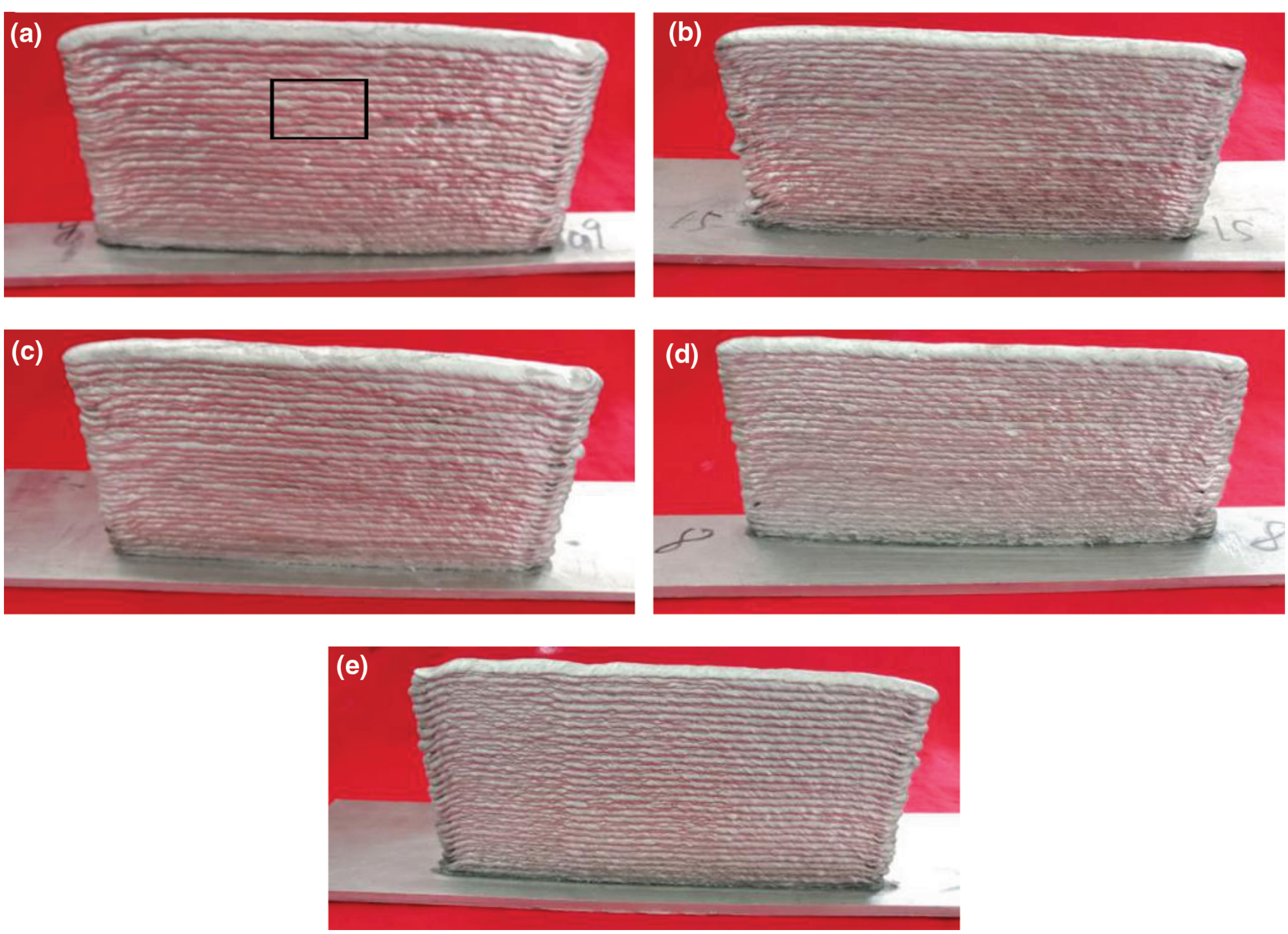

Fig. 5. The deposited sample morphology under different laser power: (a) 0 W; (b) 100 W; (c) 200 W; (d) 300W; (e) 400 W

Figure 5 shows the morphology of deposited samples with different laser power. Each sample is 30 layers, and the dimensions are shown in Table 2, L_E is the effective length of samples, W_E is the effective width of samples, and H_E is the effective height of samples. Figure 6 is side views of the marked position in Fig. 5, and we observe the sidewall from the same position in Fig. 5. Figure 6(a) shows a strong molten pool overflow. There exists a distinct stair step in Fig. 6(b)-(e), which means lower surface roughness due to the stair-stepping effect (Ref 24).

Table 2. Effective size corresponding to different parameters

Laser power, W	L_E, mm	W_E, mm	H_E, mm	EV, mm^3
0	168.04	9.87	70.89	117,574.95
100	170.15	10.26	72.53	126,618.45
200	171.63	10.31	73.57.	130,182.50
300	174.58	10.51	75.51	138,548.45
400	170.34	10.35	71.23	125,579.84

The utilization of materials is also named the deposition efficiency in the AM (Ref 25). It has been an evaluation index of AM technology. The effective area of the sample is obtained by cutting off the excess portion. As shown in Fig. 7, this is a schematic representation of the effective area of a sample. The ratio of the effective volume(EV) to the original volume of the sample(OV) is the material utilization of the sample (Ref 25). The expression of material utilization is shown in Eqs 1-5:

$$MU = EV/OV \times 100\% \quad \text{(Eq 1)}$$

$$EV = L_E \times W_E \times H_E \quad \text{(Eq 2)}$$

$$OV = S_W \times V_W \times L/V \quad \text{(Eq 3)}$$

$$S_W = \pi d^2/4 \quad \text{(Eq 4)}$$

$$L = 180n \quad \text{(Eq 5)}$$

where MU is the material utilization rate, S_W is the cross-sectional area of the wire, V_W is the wire feed speed, L is the total length of the wire used in the deposition process, V is the deposition speed, d is the diameter of the wire, and n is the number of layers of the deposited sample.

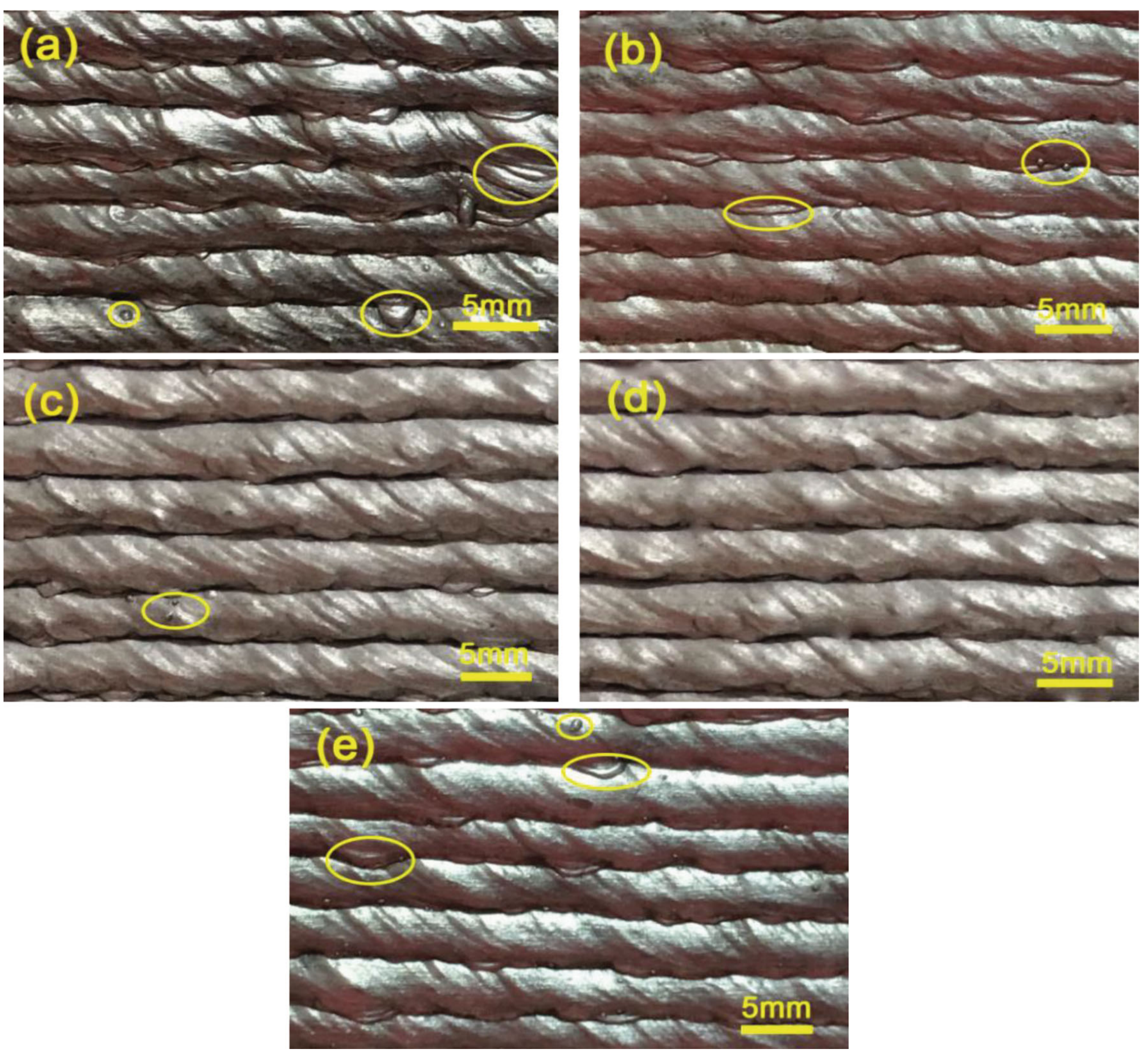

Fig. 6. Side walls quality under different laser powers: (a) 0 W; (b) 100 W; (c) 200 W; (d) 300 W; (e) 400 W

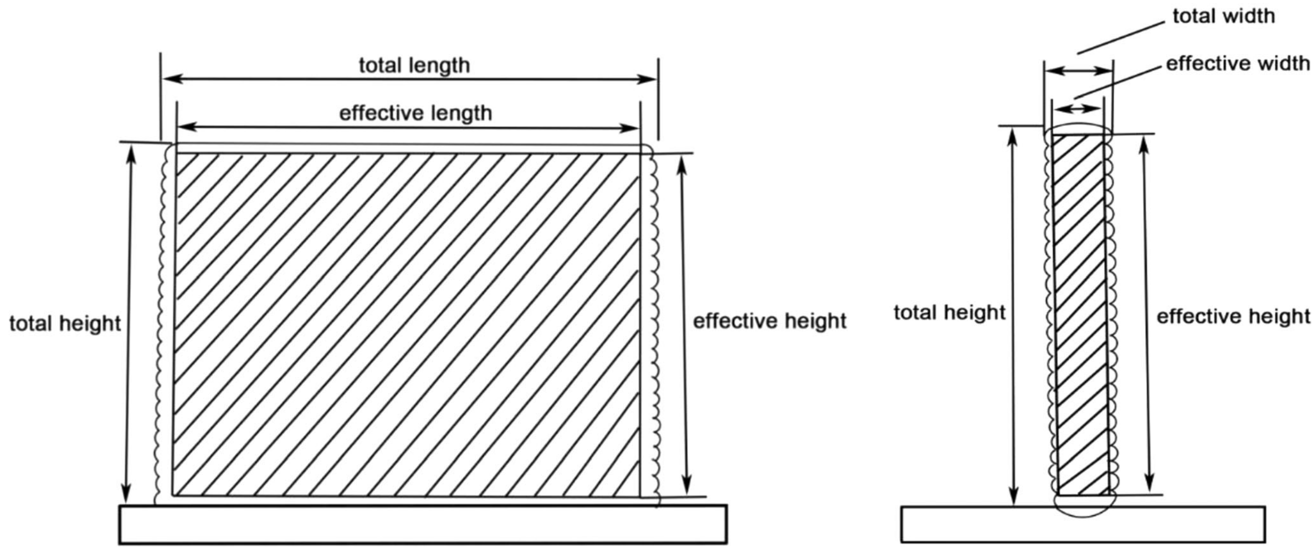

Fig. 7. Schematic diagram of the effective area of a deposited sample

After calculation, the original volume of the sample is 157,782.09 mm^3. The effective size measured by the sample of different parameters is shown in Table 2.

After calculation, the material utilization rates under different parameters are: 74.52, 80.24, 82.51, 87.81, 79.59%. When the laser power is 300 W, the value is 17.83% higher than that without laser.

After adding the laser, it can attract and compress the arc to reduce the overflow of the molten pool, and the laser can provide a stable spot for the arc (Ref 26, 27), which makes the deposited process more stable, and the surface forming quality is better than the single arc, so the deposited sample has a larger effective volume after adding the laser. However, when the laser power is too large, the heat input of the deposition process becomes large, which causes the molten pool to overflow, the surface forming quality deteriorates, and the effective volume of the sample becomes small.

3.2 Microstructure

The microstructure of deposited samples perpendicular to the scanning direction is shown in Fig. 8. It can be observed that the microstructure morphology in this zone is a typical equiaxed shape. Grain size can be recognized. Figure 8(a) is the microstructure without adding laser, the average grain size is 48.5 µm. Figure 8(b) shows the microstructure when the laser power is 100 W. The average grain size is 40.4 µm. Figure 8(c) shows the microstructure when the laser power is 200 W. The average grain size is 35.0µm. Figure 8(d) shows the microstructure when the laser power is 300 W. The average grain size is 30.8 µm, which is approximately 36.5 % smaller than that without laser. Figure 8(e) shows the microstructure when the laser power is 400 W. The average grain size is 37.5 µm.

The laser acted on the deposited metal to evaporate the metal particles, and the formed metal vapor produced an oscillating and stirring effect on the molten pool (Ref 28). And the peak laser power is larger when the laser just enters the molten pool, and there is an impact effect on the molten pool. This effect changes the surface tension of the molten pool, and the molten metal flows backwards in the molten pool and then back again (Ref 29), as Fig. 9 shows, which contributes to the fracture of dendrites and increase the nucleation points. The nucleation rate increments make the grain refined (Ref 30]. When the laser power is around 300 W, there is a balance between the stirring effect of the laser and the heat input. At this time, the grain refinement effect is better. When the laser power is increased to 400 W, the thermal input to the molten pool increases. As a result, the grain size is larger than that of the laser power of 300 W.

3.3 Tensile Tests

Figure 10 shows the tensile strength of the deposited samples under different laser power. With the increase of laser power, the tensile strength of samples increases first and then decreases in the vertical and horizontal directions. When the laser power is 300 W, the maximum ultimate strength is 268 ± 5 and 279 ± 4 MPa, which are 19 and 20.1% higher than that without laser. When the laser power is 400W, grain size becomes larger, and the tensile strength decreases in both horizontal and vertical directions. The elongation in vertical and horizontal directions is 8.89 and 9.98%, respectively, without laser. When the laser power is 300 W, the maximum elongation in vertical and horizontal directions is 10.17 and 11.71%, respectively.

The fracture surface investigated by SEM is exhibited in Fig. 11. Figure 11(a) shows the fracture surface in the horizontal direction without laser. Figure 11(b) shows the fracture surface of the tensile specimens in the horizontal direction when the laser power is 300 W. There are a large number of dimples in Fig. 11(a) and (b), and small dimples distributed around large dimples. Therefore, the fracture mode is microvoid coalescence fracture, which is a typical ductile fracture. There are pores in Fig. 11(a) and (b). These regular spherical pores' inner walls are smooth which can be judged to be hydrogen pores (Ref 28). The pores in Fig. 11(a) are

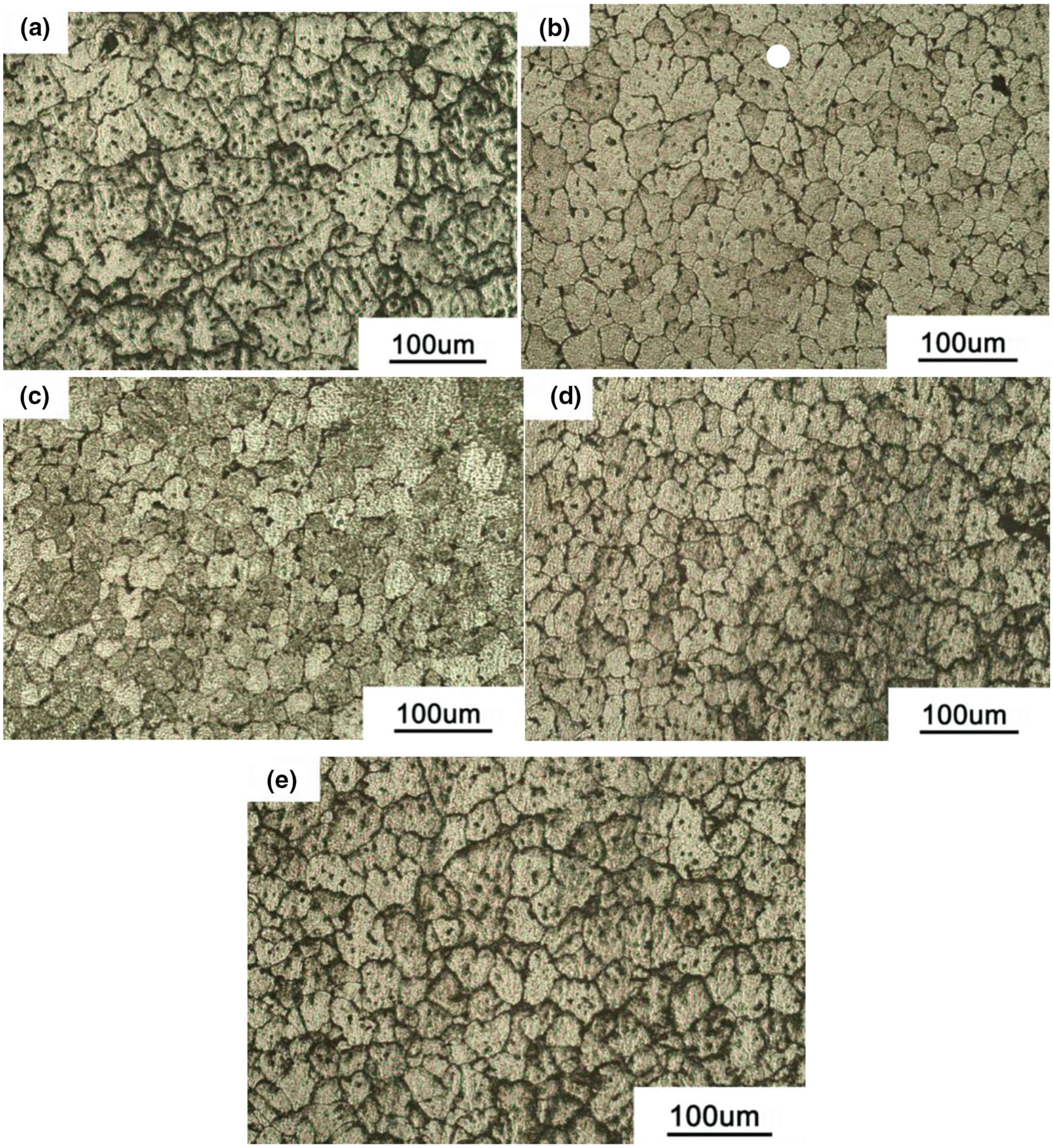

Fig. 8. Microstructure in different laser power under the OM: (a) 0 W; (b) 100 W; (c) 200 W; (d) 300W; (e) 400 W

approximately 20-50 μm in size, and the pores in Fig. 11(b) are approximately 10-30 μm in size. It is consistent with the increase in elongation after adding laser. The reason is the pulse laser can stir the molten pool, which increases the flow of the molten pool and promotes the escape of gas. It effectively reduces the internal porosity of samples (Ref 31, 32).

3.4 Micro-Hardness

Figure 12 shows the micro-hardness distribution of the samples with different laser power along the deposition direction. The red dotted lines in Fig. 13 represent the measuring position (A test point is every 0.1 mm). The hardness values of the sample change periodically along the deposition direction, which is related to the periodic distribution of the microstructure along the deposition direction (Ref 33, 34). Table 3 is the average hardness of different laser power. And micro-hardness of the sample with 300 W laser is 88.8 HV0.2, with an increase of 11.2% compared to that without laser. It is concluded that the refined grains is the main reason for the increase in microhardness. According to Hall–Petch theory, the decrease of grain size leads to the increase of grain boundary. This phenomenon is beneficial to hinder the dislocation movement, which improves the microhardness and strength (Ref 35). When the laser power is 300 W, the grain size is smaller than other samples, and the hardness of the sample is the maximum. On the other hand, some eutectic particles are dispersed inside the grain and play a role of dispersing strengthening.

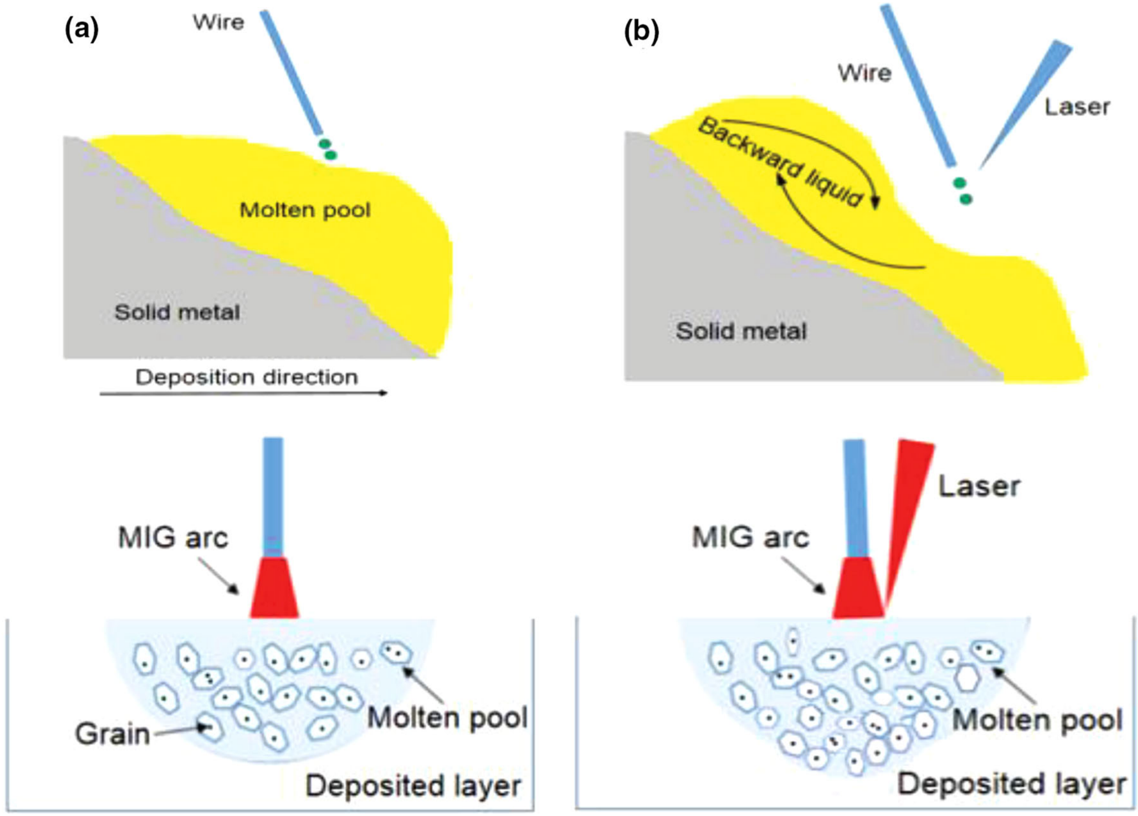

Fig. 9. The illustration of grain refinement: (a) Molten pool without laser. (b) Molten pool with laser-MIG

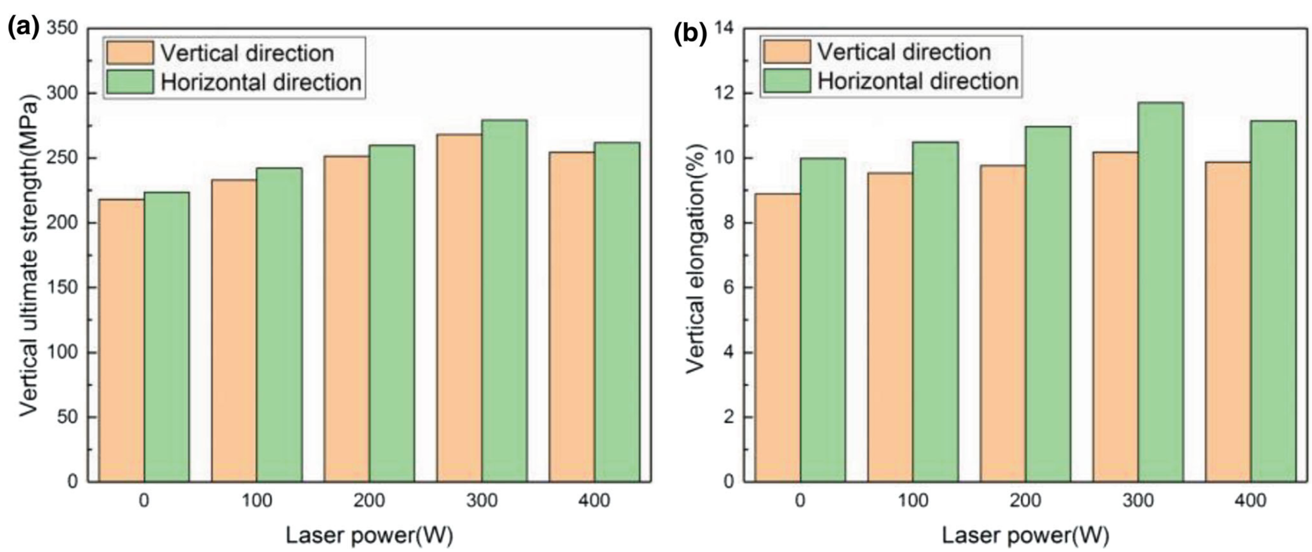

Fig. 10 Tensile properties under different laser power: (a) tensile strength; (b) elongation

3.5 The Precipitated Phase of the Additive Wall

Figure 14 shows the distribution of eutectics under SEM. It shows that a large amount of eutectics distributes on the black matrix. When there is no laser, the distribution of eutectics shows a network structure, and few eutectic particles are inside the grains. Compared with the grain morphology in Fig. 8(a), it can be concluded that these reticulated eutectics distribute along grain boundaries. The eutectic structures are refined after adding the laser (300W), and the network structures are replaced by the long striped eutectic structures.

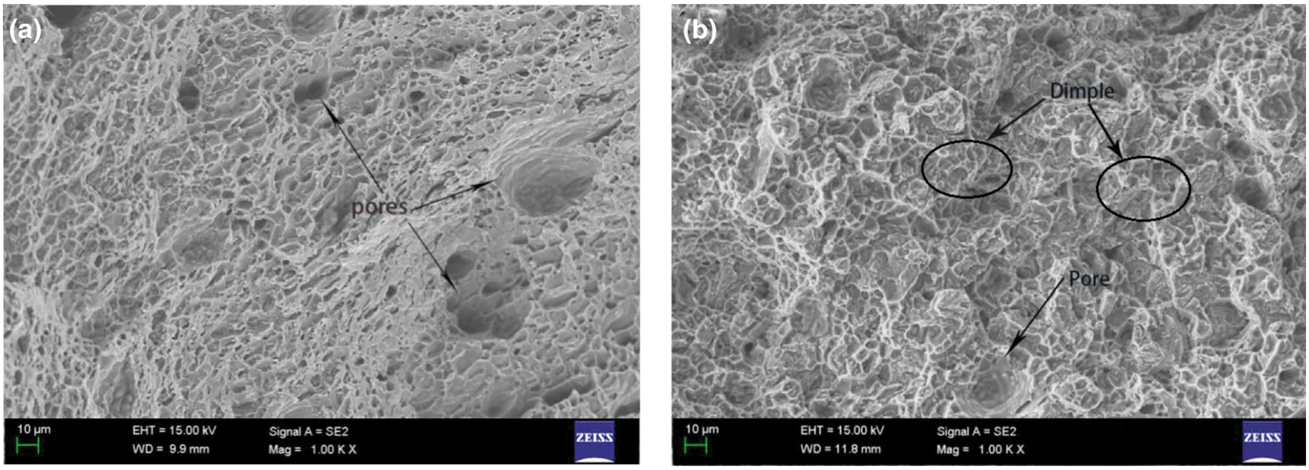

Fig. 11. Fracture morphology of the deposited samples: (a) sample without laser; (b) sample with laser power of 300 W

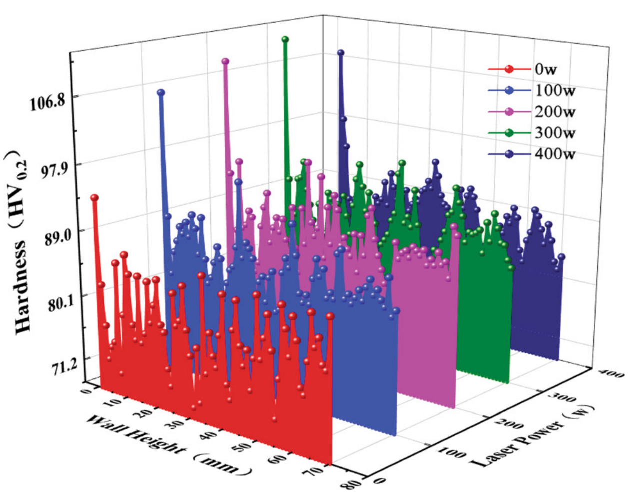

Fig. 12. Hardness distribution curve under different laser powers

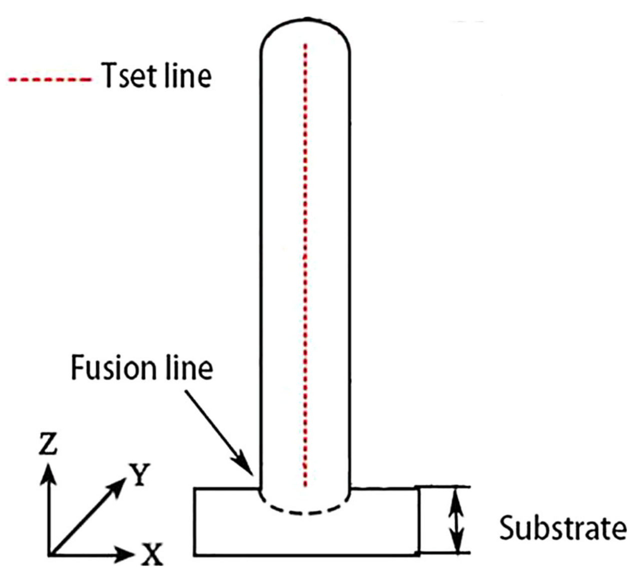

Fig. 13. Schematic diagram of the cross section of a deposited sample

Table 3 Average hardness of samples under different laser power

Laser power, W	Average hardness, $HV_{0.2}$
0	79.78
100	86.31
200	87.81
300	88.84
400	87.85

In the interior of the deposited samples, the Cu mainly solubilizes in Al matrix (Ref 28). Figure 15 shows the results of component analysis of the sample with a laser power of 300 W. As shown in Fig. 15(a) and (b), the result shows that the composition of eutectics is Al69.88Cu30.12, which is relatively close to the eutectic composition ratio of 67/33. It can be concluded that these phases are eutectic Al_2Cu, and the black matrix is Al (Ref 28).

4. Conclusions

In this study, deposited samples of different laser power are fabricated by laser-MIG hybrid additive manufacturing. The microstructure and mechanical properties of samples are investigated. The following conclusions can be obtained:

1. The utilization of materials reaches 87.81%, and the value is 17.83% higher than that without laser when the laser power is 300 W.
2. The addition of pulsed laser can refine grains and reduce porosity defects, thus improving the mechanical properties of deposited samples.
3. As the laser power increases, the hardness and tensile strength of deposited samples increase continuously, reaching the maximum values at the laser power of 300 W.

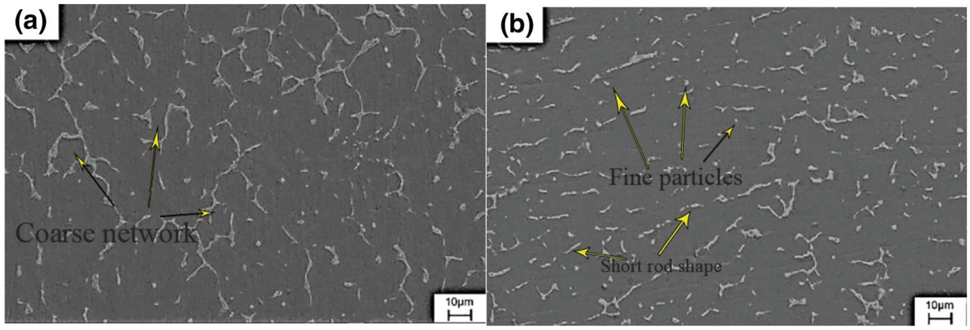

Fig. 14 The distribution of eutectic: (a) without laser; (b) with laser at 300 W power

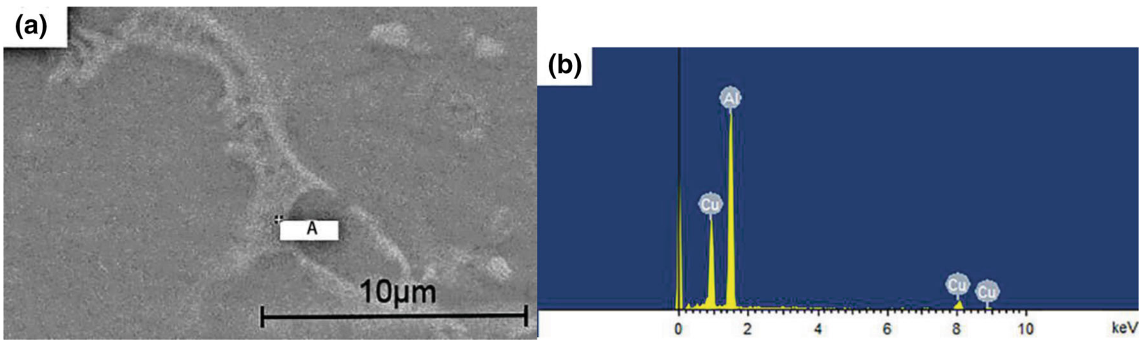

Fig. 15. Results of component analysis. (a) The test position; (b) Test results of point A

Acknowledgments

This work was supported by National Key R&D Program of China (2018YFB1107900) and Dalian High-level Talent Innovation Support Program (2017RQ102).

Conflict of interest

The authors have no conflict of interest to declare.

References

1. E.A. Starke Jr. and J.T. Staley, Application of Modern Aluminum Alloys to Aircraft, *Prog. Aerosp. Sci.*, 1996, **32**, p 131–172
2. T. Dursun and C. Soutis, Recent Developments in Advanced Aircraft Aluminium Alloys, *Mater. Des.*, 2014, **56**, p 862–871
3. Y. Zhang, L. Wu, X. Guo et al., Additive Manufacturing of Metallic Materials: A Review, *J. Mater. Eng. Perform*, 2018, **27**(1), p 1–13
4. S.H. Huang, P. Liu, A. Mokasdar and L. Hou, Additive Manufacturing and Its Societal Impact: A Literature Review, *Int. J. Adv. Manuf. Technol.*, 2013, **67**, p 1191–1203
5. F. Wang, S. Williams, P. Colegrove and A. Antonysamy, Microstructure and Mechanical Properties of Wire and Arc Additive Manufactured Ti-6Al-4V, *Metall. Mater. Trans. A*, 2013, **44**, p 968–977
6. Y. Wang, S. Konovalov, X. Chen et al., Research on Cu-6.6%Al-3.2%Si Alloy by Dual Wire Arc Additive Manufacturing, *J. Mater. Eng Perform*, 2021, **30**, p 1694–1702
7. D.H. Ding, Z.X. Pan, D. Cuiuri and H.J. Li, Wire-Feed Additive Manufacturing of Metal Components: Technologies, Developments and Future Interests, *Int. J. Adv. Manuf. Technol.*, 2015, **81**, p 465–481
8. S. Szemkus, B. Kempf, S. Jahn, G. Wiehl, F. Heringhaus and M. Rettenmayr, Laser additive manufacturing of contact materials, *J. Mater. Process. Technol.*, 2018, **252**, p 612–617
9. Q.R. Wu, Z.S. Ma, G.S. Chen, C.M. Liu, D.X. Ma and S.Y. Ma, Obtaining Fine Microstructure and Unsupported Overhangs by Low Heat Input Pulse Arc Additive Manufacturing, *J. Manuf. Process*, 2017, **27**, p 198–206
10. Y. Wang et al., Microstructure and Ratcheting Behavior of Additive Manufactured 4043 Aluminum Alloy, *J. Mater. Eng. Perform.*, 2018, **27**(9), p 4582–4592
11. M.X. Li and W.Q. Qu, Electron Beam Additive Manufacturing and its Applications in Aerospace Field, *Mater. Sci. Forum*, 2014, **789**, p 377–383
12. X.B. Gong, T. Anderson and K. Chou, Review on Powder-Based Electron Beam Additive Manufacturing Technology, *Manuf. Rev.*, 2014, **1**, p 2
13. J.H. Martin, B.D. Yahata, J.M. Hundley, J.A. Mayer, T.A. Schaedler and T.M. Pollock, 3D Printing of High-Strength Aluminium Alloys, *Nature*, 2017, **549**, p 365–369
14. M. Karg, B. Ahuja, S. Wiesenmayer, S. Kuryntsev and M. Schmidt, Effects of Process Conditions on the Mechanical Behavior of Aluminium Wrought Alloy EN AW-2219 (AlCu6Mn) Additively Manufactured by Laser Beam Melting in Powder Bed, *Micromachines*, 2017, **8**, p 23
15. S.W. Williams, F. Martina, A.C. Addison, J. Ding, G. Pardal and P. Colegrove, Wire+Arc Additive Manufacturing, *Mater. Sci. Technol.*, 2016, **32**, p 641–647
16. F. Martina, J. Mehnen, S.W. Williams, P. Colegrove and F. Wang, Investigation of the Benefits of Plasma Deposition for the Additive Layer Manufacture of Ti-6Al-4V, *J. Mater. Process. Technol.*, 2012, **212**, p 1377–1386
17. R. Li, J. Xiong and Y.Y. Lei, Investigation on Thermal Stress Evolution Induced by Wire and Arc Additive Manufacturing for Circular Thin-Walled Parts, *J. Manuf. Process.*, 2019, **40**, p 59–67
18. J.Y. Bai, C.L. Yang, S.B. Lin, B.L. Dong and C.L. Fan, Mechanical Properties of 2219-Al Components Produced by Additive Manufacturing with TIG, *Int. J. Adv. Manuf. Technol.*, 2016, **86**, p 479–485
19. B. Cong, J. Ding and S. Williams, Effect of Arc Mode in Cold Metal Transfer Process on Porosity of Additively Manufactured Al-6.3%Cu alloy, *Int. J. Adv. Manuf. Technol.*, 2015, **76**, p 1593–1606
20. Y.Y. Lei, J. Xiong and R. Li, Effect of Inter Layer Idle Time on Thermal Behavior for Multi-layer Single-Pass Thin-Walled parts in GMAW-Based Additive Manufacturing, *Int. J. Adv. Manuf. Technol.*, 2018, **96**, p 1355–1365

21. L.M. Liu, R.S. Huang, G. Song and X.F. Hao, Behavior and Spectrum Analysis of Welding Arc in Low-Power YAG-Laser-MAG Hybrid-Welding Process, *IEEE Trans. Plasma Sci.*, 2008, **36**, p 1937–1943
22. Z.D. Zhang, C.S. Sun, X.K. Xu and L.M. Liu, Surface Quality and Forming Characteristics of Thin-Wall Aluminium Alloy Parts Manufactured by Laser Assisted MIG Arc Additive Manufacturing, *Int. J. Lightweight Mater. Manuf.*, 2018, **1**, p 89–95
23. D.Q. Yang, C.J. He and G.J. Zhang, Forming Characteristics of Thin-Wall Steel Parts by Double Electrode GMAW Based Additive Manufacturing, *J. Mater. Process. Technol.*, 2016, **227**, p 153–160
24. M. Alimardani, V. Fallah, M. Iravani-Tabrizipour and A. Khajepour, Surface Finish in Laser Solid Freeform Fabrication of an AISI 303L Stainless Steel Thin Wall, *J. Mater. Process. Technol.*, 2012, **212**, p 113–119
25. Z. Zhang, C. Sun, X. Xu and L. Liu, Surface Quality and Forming Characteristics of Thin-Wall Aluminium Alloy Parts Manufactured by Laser Assisted MIG Arc Additive Manufacturing, *Int. J. Light. Mater. Manuf*, 2018, **1**, p 89–95
26. B. Hu and G. Den Ouden, Laser Induced Stabilisation of the Welding Arc, *Sci. Technol. Weld. Join.*, 2005, **10**(1), p 76–81
27. X.W. Li, G. Song and Z.D. Zhang, *Chin. J. Lasers*, 2019, **46**(12), p 1202006
28. D.J. Wu, D.H. Liu, F.Y. Niu et al., Al–Cu Alloy Fabricated by Novel Laser-Tungsten Inert Gas Hybrid Additive Manufacturing, *Addit. Manuf.*, 2020, **32**, p 10054
29. H. Rao, S. Giet, K. Yang et al., The Influence of Processing Parameters and Aluminium alLoy A357 Manufacturing by Selective Laser Melting, *Mater. Des.*, 2016, **109**, p 334–346
30. G.D. Janaki Ram, R. Murugesan and S. Sundaresan, Fusion Zone Grain Refinement in Aluminum Alloy Welds Through Magnetic Arc Oscillation and Its Effect on Tensile Behavior, *J. Mater. Eng. Perform.*, 1999, **8**, p 513–520
31. Q.Y. Miao, D.J. Wu, D.S. Chai et al., Comparative Study of Microstructure Evaluation and Mechanical Properties of 4043 Aluminum Alloy Fabricated by Wire-Based Additive Manufacturing, *Mater. Des.*, 2020, **186**, p 234–246
32. B. Wang, G.W. Ran and G.Y. Xue, Welding Technology and Joint Properties of the High Strength Aluminum Alloy by Laser-Assisted TIG Arc Weldin, *Weld. Technol.*, 2012, **41**(7), p 22–26
33. N.Q. Wu, C. Xia, M. Li, N. Perrusquia and S.X. Mao, Interfacial Structure and Micro and Nano-mechanical Behavior of Laser-welded 6061 Aluminum Alloy Blank, *J. Eng. Mater. Technol.*, 2004, **126**, p 8–13
34. E.L. Stevens, J. Toman, A.C. To and M. Chmielus, Variation of Hardness, Microstructure, and Laves Phase Distribution in Direct Laser Deposited Alloy 718 Cuboids, *Mater. Des.*, 2017, **119**, p 188–198
35. M. Furukawa, Z. Horita, M. Nemoto, R.Z. Valiev and T.G. Langdon, Microhardness Measurements and the Hall–Petch Relationship in an Al-Mg Alloy with Submicrometer Grain Size, *Acta Mater.*, 1996, **44**, p 4619–4629